ADVANCED FUNCTIONAL MATERIALS
www.afm-journal.de

Materials Views
www.MaterialsViews.com

Combinatorial Atmospheric Pressure Chemical Vapor Deposition of F:TiO_2; the Relationship between Photocatalysis and Transparent Conducting Oxide Properties

*Andreas Kafizas, Nuruzzaman Noor, Penelope Carmichael, David O. Scanlon, Claire J. Carmalt, and Ivan P. Parkin**

Combinatorial atmospheric pressure chemical vapor deposition (APCVD) is used to deposit anatase TiO_2 with a graded level of F-doping between 1.10 ≤ F:Ti (at%) ≤ 2.57 from the reaction of titanium tetrachloride, ethyl acetate and trifluoroacetic acid at 500 °C on glass. The photocatalytic activity and electrical resistivity of 200 allotted positions across a grid are screened using high-throughput techniques. A blue region of film is singled out for containing the lowest electrical resistivities of any previously reported doped or undoped TiO_2-based system formed by APCVD ($\rho \approx 0.22$–$0.45\ \Omega$ cm, n = 0.8–1.2×10^{18} cm^{-3}, $\mu = 18$–33 cm^2 V^{-1} s^{-1}). The blue region contains a lower fluorine doping level (F:Ti ≈ 1.1–1.6%, $E_{bg} \approx 3.06$ eV) than its neighboring colorless region (F:Ti ≈ 2.3–2.6%, $E_{bg} \approx 3.15$–3.21 eV, $\rho \approx 0.61$–$1.3\ \Omega$ cm). State-of-the-art hybrid density functional theory calculations were employed to elucidate the nature of the different doping behaviors. Two distinct fluorine doping environments were present. At low concentrations, F substituting for O (F_O) dominates, forming blue F:TiO_2. At high concentrations, negatively charged fluorine interstitials (F_i^{-1}) begin to dominate, forming transparent F:TiO_2.

1. Introduction

TiO_2 thin-films have been the subject of extensive study due to their multi-functional application in photocatalysis,[1,2] water-splitting,[3–5] gas-sensing,[6] and more.[7] The majority of research has focused on improving the photocatalytic efficiency under visible/solar conditions by doping or forming a composite material.[8–12] Of late, there has also been increasing interest in improving the material's electrical properties for optoelectronic applications.[13–19] Given the chemical, acid and long-term humidity resistance of TiO_2, the benefits for improving the electrical properties are clear when compared with traditional transparent conducting oxide (TCO) materials such as In_2O_3, SnO_2, CdO, and ZnO.

Fluorine doping of TiO_2 (F:TiO_2) has been shown to enhance visible light photocatalysis in powders,[20–22] nanotubes[23,24] and thin-films.[25–28] The mode of enhancement has been attributed to a red-shifted bandgap, the creation of surface oxygen vacancies, the enhancement of surface acidity and the increase of Ti^{3+} states.[29] The gas sensing[30] and optical[31–33] properties of F:TiO_2 thin-films have also been studied. Recently, it has also been shown that electrical resistivities ($\rho = 1.6 \times 10^{-3}\ \Omega$ cm) not far from fluorine doped tin oxide ($\rho \approx 5$–$6 \times 10^{-4}\ \Omega$ cm[34–36] can be achieved in F:TiO_2 thin-films grown by an optimized physical layer deposition (PLD) process.[15]

F:TiO_2 thin-films have mostly been synthesized by sol-gel,[25,27] hydrothermal,[28,30] and physical vapor deposition (PVD) routes.[15,32,33] Interestingly, thin-films of F:TiO_2 have not previously been grown by chemical vapor deposition (CVD) and in this article we demonstrate the first such case at atmospheric pressure.

Atmospheric pressure chemical vapor deposition (APCVD) is used to produce high quality and conformal TiO_2 thin-films on the minute time-scale.[37] Crucially, TiO_2 thin-films with significant variations in phase, thickness and doping level can be achieved using combinatorial APCVD (cAPCVD).[13,16,17,38–41] Traditionally, precursor gas flows are homogenized before entering the reactor, whereas in cAPCVD precursors are introduced at separate points.[42] This creates a precursor gradient across the reactor, inducing combinatorial film growth and producing a film with such a variety of make-up that different

Dr. A. Kafizas
Department of Chemistry
Imperial College London
Exhibition Road, London, SW7 2AZ, UK
N. Noor, P. Carmichael, Dr. D. O. Scanlon,
Prof C. J. Carmalt, Prof. I. P. Parkin
Materials Chemistry Research Centre
Department of Chemistry
University College London
20 Gordon Street, London, WC1H 0AJ, UK
E-mail: i.p.parkin@ucl.ac.uk
Dr. D. O. Scanlon
Diamond Light Source Ltd.
Diamond House Harwell Science, and Innovation
Campus Didcot Oxfordshire OX11 0DE, UK

DOI: 10.1002/adfm.201301333

functional properties can be observed at distinct points along the film. cAPCVD is a relatively new synthetic technique that has primarily been used to understand the relationship between composition and function in a number of systems.[13,16,17,38–41,43] For instance, in one study, the simultaneous investigation of a range of anatase: rutile TiO_2 composite states grown across a single thin-film showed how the much debated photocatalytic synergy of the two phases is not present in thin-film form.[41] The convenience of having such a variety of unique materials grown over a single film is two-fold. Firstly, only one synthesis is required. Secondly, the increased sensitivity, speed and availability of modern characterization methods can be exploited and a large body of unique states can be rapidly characterized and inter-related.

Applying a combinatorial approach allowed us to investigate 200 unique states formed across a F:TiO_2 system. The positions were screened using tailored high-throughput methods, revealing a blue patch of film with enhanced electrical conduction ($\rho \approx 0.22$–$0.45\ \Omega$ cm) that hitherto has not been reported. A single horizontal strip of film that encompassed both blue and transparent sections of the film was investigated in greater detail in order to determine: (i) why a blue region forms, (ii) why electrical conductivity is greater in the blue region, and (iii) why photocatalysis was lower in the blue region. To complement our combinatorial approach, a hybrid density functional theory (DFT) investigation of the interaction of fluorine dopants in bulk anatase TiO_2 was conducted, revealing a strong dependence of the dominant defect mechanism on the doping level. Moreover, the calculations showed how F atoms substitute O sites (F_O) at low doping levels, forming blue F:TiO_2, but at higher doping levels negatively charged fluorine interstitials (F_i^{-1}) begin to dominate, forming transparent F:TiO_2.

2. Results and Discussion

2.1. Physical Characterization

An anatase TiO_2 thin-film with a fluorine doping gradient (F:TiO_2) was synthesized by cAPCVD on glass. The system was designed to produce compositional and thickness gradients across the substrate to rapidly allow access to a wide range of composition and phase-space in a single experiment. The synthetic process involved the reaction of titanium tetrachloride ($TiCl_4$) [the Ti source] with ethyl acetate [the O source] and trifluoroacetic acid [the F source] at 500 °C; coating the entire glass substrate. The film showed color bands when viewed off-angle due to the variation in film-thickness, characteristic of thin-films with high refractive indices.[13] The color bands alternated chiefly from green to pink to a point located within the middle-left section of the film (i.e., the thickness maximum). Interestingly, this also corresponded with the unexpected formation of a dark blue patch (**Figure 1**). This blue color was seen at all viewing angles (i.e., not an interference effect) and was intrinsically due to F-doping. The film was adhesive, passing the Scotch tape test, resisted scratching with a steel scalpel and indefinitely stable in air over several months.

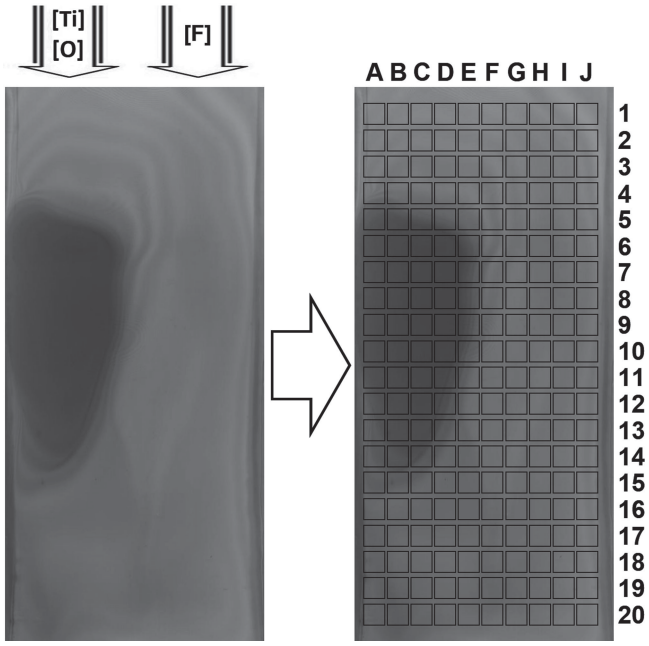

Figure 1. Left: Photograph of the F:TiO_2 thin-film formed from the combinatorial APCVD of titanium tetrachloride, ethyl acetate and trifluoroacetic acid at 500 °C with the relative point of entry of each precursor shown above. Right: a superimposed grid reference of the 200 positions probed by our screening tools (neighboring grid positions are spaced ≈ 0.75 cm apart from centre to centre).

2.2. Rapidly Probing the Material for Functional Trends

Rather than laboriously characterize the entire material by traditional methods, we instead quickly probed a large number of locations using fast-mapping tools to discover regions of interest, which were later investigated in greater detail. In this case we applied three such tools to determine: (i) film-thickness, (ii) photocatalytic activity, and (iii) electrical resistance across 200 positions on a grid (Figure 1).

2.2.1. Film Thickness

The alternating color bands observed across the film were due to variations in material thickness (Figure 1). Such bands are observed in TiO_2 when films range in thickness from ≈0.1–10 μm.[13] The effect is due to the series of constructive and destructive interferences of light as it passes through a smooth and transparent medium. The reflectance/transmittance spectroscopy of such materials reveals a series of undulations when the conditions for constructive and destructive interference are met and gives rise to the variety of colors seen off-angle in TiO_2. The thickness can be determined spectroscopically if the spectral dependence of the refractive index is known.[44] The film-thickness was thus determined spectroscopically by applying the Swanepoel method.[45] This was achieved using an automated method that (i) measured the optical reflectance over 300–1000 nm using a fiber optic and (ii) fit the wave-patterns to a thickness model; this required less than 3 seconds of analysis per grid-position. Example wave-patterns for the

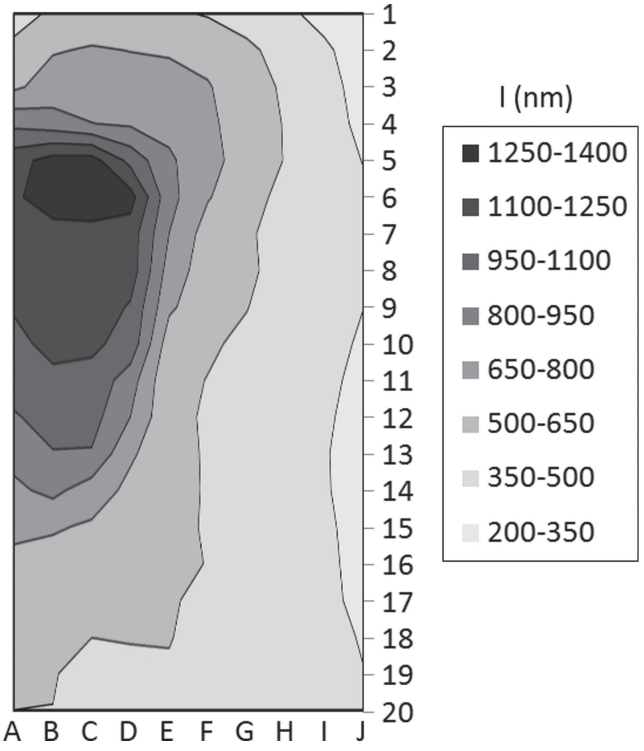

Figure 2. A 3D contour map of film-thickness (nm) for all 200 grid-positions across the combinatorial F: TiO_2 thin-film.

10 positions across Row 8 are shown in the Supporting Information (S1) and a 3D contour map of film-thickness for all 200 grid-positions is shown in **Figure 2**. Film-thicknesses ranged from 230 to 1320 nm, maximizing where the color bands accumulated in the middle-left blue portion of film (position B6 being the thickest point) and minimizing on the right side of the film (Column J).

2.2.2. Photocatalytic Activity

The photocatalytic activity at each of the 200 allotted grid-positions was determined using a screening method that relies on digital photography to monitor the reaction progression.[46,47] The film was first coated with an even layer of a resazurin-based intelligent ink.[48] The ink-coated film was then exposed to UVA radiation in intervals, with regular breaks for each photograph to be taken. The UVA light instigated a photocatalytic reduction of the dye by the F:TiO_2, causing it to change color from royal blue (resazurin) to pink (resorufin) to colorless (di-hydro resorufin); each a one-proton-one-electron process (**Scheme 1**).

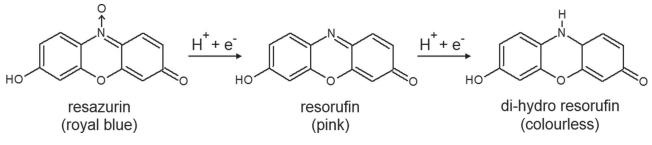

Scheme 1. The associated changes in the redox dye resazurin (royal blue) during its photocatalytic reduction to resorufin (pink) and di-hydro resorufin (colorless).

The dye first turned pink on the outer-edges of the film, primarily in the top and bottom-left regions where the film was thinnest. This occurred after ≈35–50 min of exposure to UVA light. This trend continued upon further exposures, with most of the dye turning colorless in these regions after ≈140 min. At this point, the dye starting turning pink in the thicker regions of the film and by 280 min had turned the dye colorless. By eye, the change in color in the dark blue region of film was not obvious given the dark background. However, these changes were picked up readily by the digital RGB Extractor color analysis system.[49] A reaction time-line of some selected photos is supplied in the Supporting Information (S2). As the ink alone is stable to several hours of such UVA exposure, the degradation of the dye was attributed to photocatalysis alone.[46] The rate of photocatalysis was determined by modeling the changes in digital color. Previous kinetic studies have shown that changes in the red component of digital color are directly related to the conversion of resazurin to resorufin.[46,47] Therefore, changes in the red component of digital color at each of the 200 allotted grid-positions were extracted from each photo.[49] By fitting the changes in the red component of digital color to a Boltzmann model,[50] the time taken for the complete conversion of resazurin to resorufin was determined at each grid position. By knowing how thick the ink layer was, these times could be converted into photocatalytic rates (molecules reduced cm^{-2} s^{-1}). After measuring the photon flux experienced at each grid position ($\mu = 3.47 \times 10^{14}$; $\sigma = 2.33 \times 10^{13}$ photons cm^{-2} s^{-1}), the formal quantum efficiency (FQE = molecules degraded/incident photon) was determined. Moreover, by assuming the level of UVA light absorbed by this indirect bandgap semiconductor varied in accordance with the following equation:[41]

$$\text{UVA(\%)absorbed} = 0.0531 \times \text{film} - \text{thickness(nm)} \quad (1)$$

The formal quantum yield (FQY = molecules degraded/photon absorbed) was also determined. A 3D contour map of the FQY (10^{-5}) is shown in **Figure 3**.

The FQY was lowest in the dark blue region of the film (middle-left; FQY $\approx 1 \times 10^{-4}$) and highest in the thinnest and most transparent sections (top, right, and bottom edges; FQY $\approx 2 \times 10^{-3}$). As such, thinner sections of the film transferred photogenerated electrons onto resazurin dye molecules with greatest efficiency. The relationship between film-thickness and FQY followed an exponential decay curve. A plot of the natural logarithm of FQY and film-thickness is provided in the Supporting Information (S3). The FQYs observed across this F:TiO_2 system were lower than those previously observed for the same reaction on undoped TiO_2 made analogously by APCVD (FQY = 2.5×10^{-2}).[41] This suggested fluorine doping causes a reduction in UVA photocatalysis; a case similar to that of nitrogen doping.[17]

2.2.3. Electrical Resistance

Electrical resistance ($\Omega/\square$) was measured at each of the 200 grid positions by translating a four-point probe across the surface. By measuring changes in voltage and current the sheet resistance was determined using the following equation:[51]

$$\textit{sheet resistance}\left(\frac{\Omega}{\square}\right) = 4.53 \times \frac{\textit{Voltage}\ (V)}{\textit{Current}\ (A)} \quad (2)$$

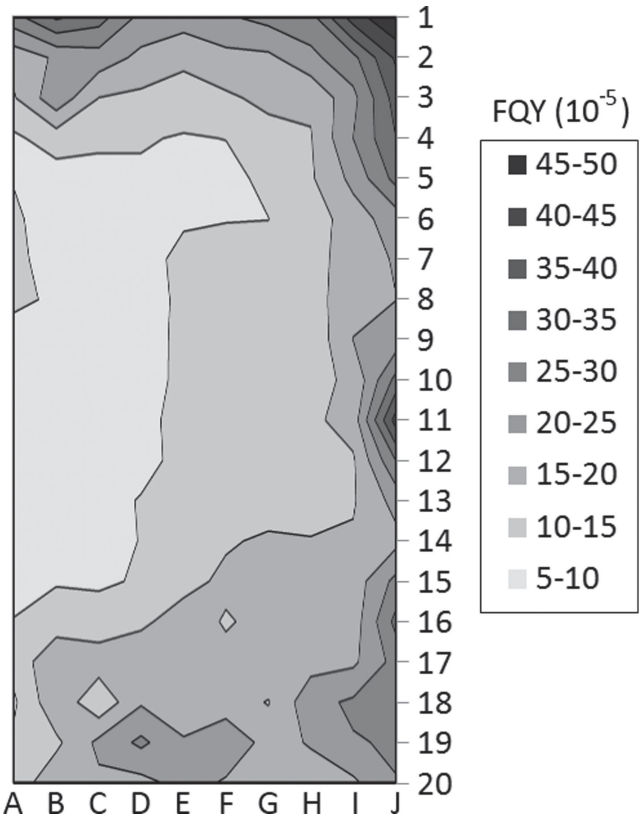

Figure 3. 3D contour map of the formal quantum yield (FQY = molecules degraded/photon absorbed) for the 200 allotted grid-positions across the combinatorial F:TiO_2 thin-film.

A 3D map of sheet resistance (Ω/□) was generated, shown in **Figure 4**(a). Resistances varied from 1200 to 81 000 Ω/□. In order to show that the increase in conductivity was not merely due to an increase in the number of electron paths (i.e., film thickness), this effect was removed by deriving electrical resistivity (ρ = Ω cm):

$$resistivity\,(\Omega.\mathrm{cm}) = sheet\,resistance\left(\frac{\Omega}{\square}\right) \times thickness\,(cm) \quad (3)$$

With knowledge of film-thickness, the resistivity (Ω cm) was determined and a 3D map drawn (Figure 4(b)). No lasting relationship between film-thickness and electrical resistivity was observed. The resistivity was lowest in the dark blue region of film, minimizing at position C8 (ρ = 0.15 Ω cm) and highest in the transparent region of film, maximizing at position J2 (ρ = 1.98 Ω cm). The resistivity values achieved were lower than the optimum values achieved in similar APCVD studies of metal-ion doped TiO_2 (W:TiO_2, ρ = 0.19 Ω cm;[13] Nb:TiO_2, ρ = 0.22 Ω cm).[16]

Using these simple techniques we were able to rapidly screen the photocatalytic and electrical properties of 200 select positions across a combinatorial F:TiO_2 system. In order for fair comparisons to be made (i.e., deriving the FQY and electrical resistivity), film thickness had to be accounted for.

It was within the dark blue region of film that the lowest electrical resistivity was observed. On the other hand, the lowest photocatalytic efficiency was observed there too. Overall, a trade-off between low electrical resistance and high UVA photocatalytic activity was present in this system. In order to acquire a better understanding of this effect, the 10 grid-positions that lay across Row 8 were investigated in greater detail. Furthermore a series of computational calculations were employed to identify the nature of the fluorine dopant.

2.3. Understanding the Physical Reasons Behind the Observed Functional Trends

There are often a number of physical properties that contribute to any given functional effect. For instance, the photocatalytic activity of a thin-film is primarily governed by: (i) the bandgap energy, (ii) film-thickness, (iii) surface topography, (iv) film-crystallinity and (v) the number of active surface sites.[1] The electrical conductivity of a thin-film is principally governed by the number of charge carriers (n) present and their mobility (μ). The physical properties that control these two factors are: (i) the dopant level (i.e., charge carrier injection), (ii) crystal defects and grain boundaries, (iii) surface microstructure, (iv) film-thickness, and (v) film crystallinity.

Within the combinatorial F: TiO_2 system, a wide range of photocatalytic activities (Figure 3) and electrical resistivities (Figure 4) were observed. Row 8 was investigated in greater detail as it encompassed both blue and transparent sections of film and contained the most electrical conductive sample (C8, ρ = 0.15 Ω cm).

2.3.1. X-Ray Crystallography

X-ray diffraction patterns revealed the exclusive formation of anatase TiO_2 ($I4_1/amd$)

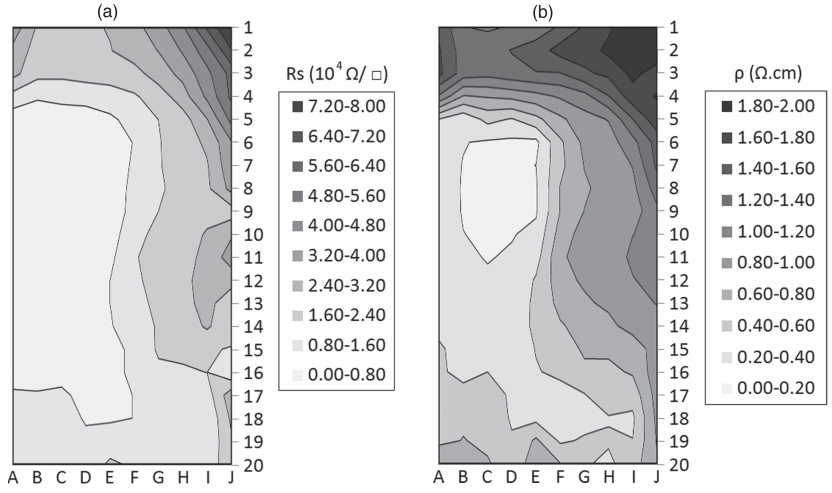

Figure 4. 3D contour maps of a) sheet resistance [Rs (10^4Ω/□)] and b) electrical resistivity [ρ (Ω cm)] for the 200 allotted grid positions across the combinatorial F:TiO_2 thin film.

Table 1. An amalgamation of physical and functional data of the 10 grid positions located across Row 8 acquired from a range of analysis methods including X-ray diffraction (XRD), X-ray photoelectron spectroscopy (XPS), UV-visible spectroscopy, Van der Pauw and Hall Effect electrical measurements, and photocatalytic efficiency to the reduction of a resazurin-based ink.

Grid Position	Physical Properties										Functional Properties					
	XRD				XPS	Spectroscopy					Electrical				Photocatalysis	
	a [Å]	c [Å]	Volume [Å^3]	τ [nm][a)]	F/100 Ti	Bandgap [eV]	l [nm][b)]	n[c)]	α [cm^{-1}][c)]	T [%] @ 2500 nm	Van der Pauw Resistivity [Ω cm]	Hall[d)]	FQE (10^5) n [10^{17} cm^{-3}]	FQY (10^5) μ [cm^2 V^{-1}s^{-1}]		
A8	3.7975 (2)	9.5181 (2)	137.23 (1)	94 (5)	1.24 ± 0.12	3.062 (1)	967	3.00	3960	4.1	0.27	0.45	−8.4	18	6.7 ± 1.0	11.3 ± 1.7
B8	3.7980 (2)	9.5212 (2)	137.34 (1)	91 (5)	1.10 ± 0.21	3.060 (1)	998	3.16	4320	2.9	0.19	0.22	−8.4	33	5.8 ± 0.87	9.0 ± 1.4
C8	3.8006 (2)	9.5217 (2)	137.54 (1)	89 (5)	1.44 ± 0.10	3.058 (1)	1025	3.03	4590	2.0	0.15	0.23	−9.4	29	4.9 ± 0.73	7.7 ± 1.1
D8	3.8002 (2)	9.5260 (1)	137.57 (1)	103 (6)	1.60 ± 0.23	3.064 (1)	912	3.22	5230	3.0	0.16	0.29	−12	19	4.6 ± 0.70	7.4 ± 1.1
E8	3.8014 (2)	9.5318 (2)	137.74 (1)	64 (4)	2.24 ± 0.08	3.083 (1)	793	2.83	4520	8.3	0.18	0.26	−3.7	67	4.4 ± 0.66	11.2 ± 1.7
F8	3.8050 (1)	9.519 (1)	137.82 (2)	49 (3)	2.52 ± 0.15	3.154 (1)	653	2.37	1380	38	0.61	*br*	*br*	*br*	3.9 ± 0.58	12.7 ± 1.9
G8	3.8001 (2)	9.592 (4)	138.51 (6)	48 (3)	2.30 ± 0.28	3.177 (1)	557	2.39	1410	42	0.78	*br*	*br*	*br*	3.3 ± 0.49	11.8 ± 1.8
H8	3.8016 (2)	9.635 (4)	139.25 (6)	37 (2)	2.44 ± 0.23	3.188 (1)	452	2.42	1970	43	0.87	*br*	*br*	*br*	3.1 ± 0.47	12.7 ± 1.9
I8	3.8034 (2)	9.633 (5)	139.36 (7)	41 (2)	2.44 ± 0.09	3.200 (1)	413	2.49	2500	46	0.95	*br*	*br*	*br*	4.1 ± 0.62	18.4 ± 2.8
J8	3.8060 (2)	9.631 (2)	139.51 (4)	45 (3)	2.57 ± 0.07	3.210 (1)	368	2.35	2350	46	1.3	*br*	*br*	*br*	4.0 ± 0.60	19.9 ± 3.0

[a)]τ = average crystallite size; [b)]l = film-thickness; [c)]average between 500 and 1000 nm; [d)]*br* = beyond range of detection. Numbers in parentheses represent the error on the last digit.

[see Supporting Information (S4)]. However, both the degree of preferred crystal orientation and the unit cell (**Table 1**) changed significantly across the row. Distinct trends were observed. For instance, the unit cell volume increased across the row. More specifically, a sharp increase in unit cell volume was observed on movement from the blue region into the transparent region of film. This was due primarily to a large increase in the *c* axis, increasing by 1.2% on movement from F8 (*c* = 9.519 (1) Å) to H8 (*c* = 9.635 (4) Å). The average crystallite size, determined by the Scherrer method,[52] was between ≈90 and 100 nm within the deep-blue region of film (grid-positions A8 to D8) and between ≈40 and 50 nm within the transparent region (grid positions F8 to J8). An intermediate crystallite size of ≈60 nm was observed at grid-position E8, a site located between the two regions where the blue region began to fade. Stark changes in preferred crystal growth were also observed on movement out of the blue region into the transparent region. As such, the degree of change in preferred growth relative to a single crystal of anatase TiO_2 was also determined [see Supporting Information (S5)].

Within the blue region, the greatest increase in preferred growth relative to a single crystal was in the (004) plane (≈60% increase). On moving out of the blue region, the growth in the (004) plane was inhibited when compared with the single crystal, with an ≈60% decrease seen at grid-position E8. On reaching the transparent region (grid positions G8 to J8), growth in the (004) plane was entirely inhibited. A similar trend was observed for growth in the (105) plane, being prominent for locations within the blue region and inhibited for locations within the more transparent region. An inverse trend was observed for growth in the (211) plane. Growth in the most prominent (101) diffraction peak of anatase TiO_2 was inhibited across the board with a less inhibited growth observed in the transparent region (≈20% decrease) compared with the blue region (≈60% decrease).

2.3.2. Raman Spectroscopy

The Raman spectrum was measured for the 10 grid-positions along Row 8. Similar to X-ray crystallography studies, the exclusive formation of anatase TiO_2 was observed. The prominent E_g band was present at ≈148 cm^{-1} and less intense bands at ≈200 (E_g), ≈394 (B_{1g}), ≈517 (A_{1g} + B_{1g}) and ≈638 cm^{-1} (B_{1g}).[53] The position of the principle E_g mode did not change significantly across the row (148 ± 0.4 cm^{-1}) but was consistently higher than un-doped anatase TiO_2 (144 cm^{-1});[53,54] a change often associated with doping.[55] Interestingly, there was a regular peak shift across the row; the biggest shifts being present in the A_{1g} + B_{1g} (516.4 to 519.2 cm^{-1}) and B_{1g} bands (637.1 to 638.4 cm^{-1}). As the position of a Raman mode is a function of the atomic positions within the crystal, these changes were plotted against unit cell volume (**Figure 5**). Two linear relationships were observed. With increasing unit cell volume, the energy of the A_{1g} + B_{1g} band increased (r^2 = 0.86). Conversely, with increasing unit cell volume the energy of the E_g band decreased (r^2 = 0.90). Moreover, the biggest increase in energy was within the A_{1g} + B_{1g} band, which is generated solely from vibrations in the *c* axial direction;[54] the axis in which unit cell expansion was greatest.

2.3.3. X-Ray Photoelectron Spectroscopy

The level of fluorine doping was determined by X-ray photoelectron spectroscopy (XPS). As XPS is a surface sensitive technique,[56] the surface was sputtered and analyzed for several cycles in order to compare the surface and bulk doping level. No surface segregation effects were observed, indicating

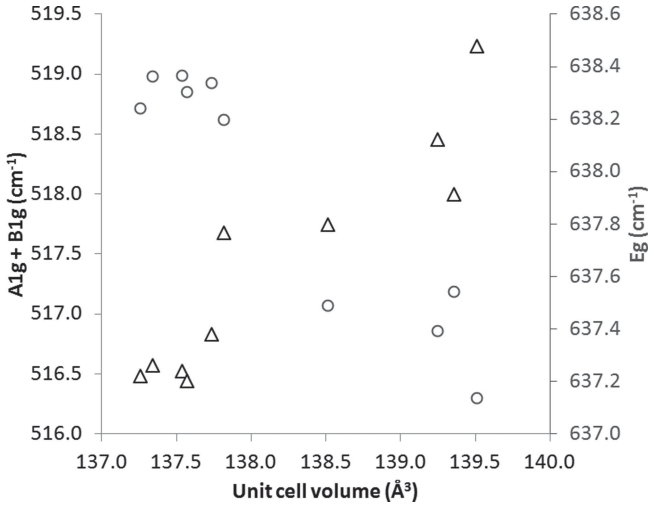

Figure 5. A direct comparison of unit cell volume (Å^3) and shift in Raman vibrational mode for the A_{1g} + B_{1g} (≈517 cm^{-1}, triangles) and E_g (≈638 cm^{-1}, circles) bands for the 10 grid positions located across Row 8 in the combinatorial F:TiO_2 thin film.

a homogenous incorporation of fluorine during film growth. Notably, the XPS depth profile showed only Ti, O, and F were present in the bulk, with other impurity elements such as C being below the detection limits. However, the fluorine to titanium ratio differed across the row (Table 1). A trend was observed where the fluorine level (per 100 Ti atoms) increased almost linearly from grid-position A8 (1.24 ± 0.12) to F8 (2.52 ± 0.15) and then plateaued (**Figure 6**(a)).

A steep increase in fluorine dopant level occurred on movement from the blue region (grid positions A8 to D8) into the transparent region (grid positions F8 to J8). The unit cell continued to expand from grid-position F8 to J8 (Table 1), even though the fluorine dopant level had reached a plateau. In addition, a decrease in the Ti 2p binding energy occurred on movement from the blue region to the more transparent region (Figure 6(b)). Of note, the binding energy in the blue region was more cationic (i.e., more strongly Ti^{4+}), therefore the blue coloration was not attributed to the presence of Ti^{3+} ions.[57] In the blue region of film, the F 1s binding energy was 684.8 eV on average. However, in the transparent region of film, the F 1s binding energy decreased to 684.5 eV on average. Blue-colored F:TiO_2 has not previously been reported.[20,22,24,27,58–60] A range of F 1s binding energies have been observed in the literature. Todorova et al. showed that nanocrystalline F:TiO_2 powders formed by sol-gel possessed a F 1s binding energy of 684.3 eV; attributed to F^- ions chemically likened to TiF_4.[20] However, Xu et al. attributed the two F 1s environments in their F:TiO_2 sol–gel films of 684.3 eV and 688.4 eV to surface bound fluorine and F^- ions that substitute O^{2-} sites respectively.[27] There was clearly inconsistency in the literature, with F 1s energies between 684.1–685.3 eV attributed to F^- in some cases[20,22,24,60] and surface bound fluorine in others.[27,58,59] In this study, each sample was probed several nanometers deep using Ar ion sputtering. As such, the binding energies were representative of fluorine sites located in the bulk. There was agreement with the studies of Di Valentin et al. who showed through XPS depth profiling and EPR studies that two distinct F^- doping sites were present in F:TiO_2 at 684.1 eV and 685.3 eV.[60] Two distinct fluorine dopants were present in our system, one being more prominent in the blue region and the other being more prominent in the transparent region.

2.3.4. Scanning Electron Microscopy

The effect on crystal growth was further explored by scanning electron microscopy (SEM) studies. Images are provided in the Supporting Information (S6). The individual crystals were of a similar size to those determined from line-broadening studies of X-ray crystal data (Table 1), which indicated that each grain

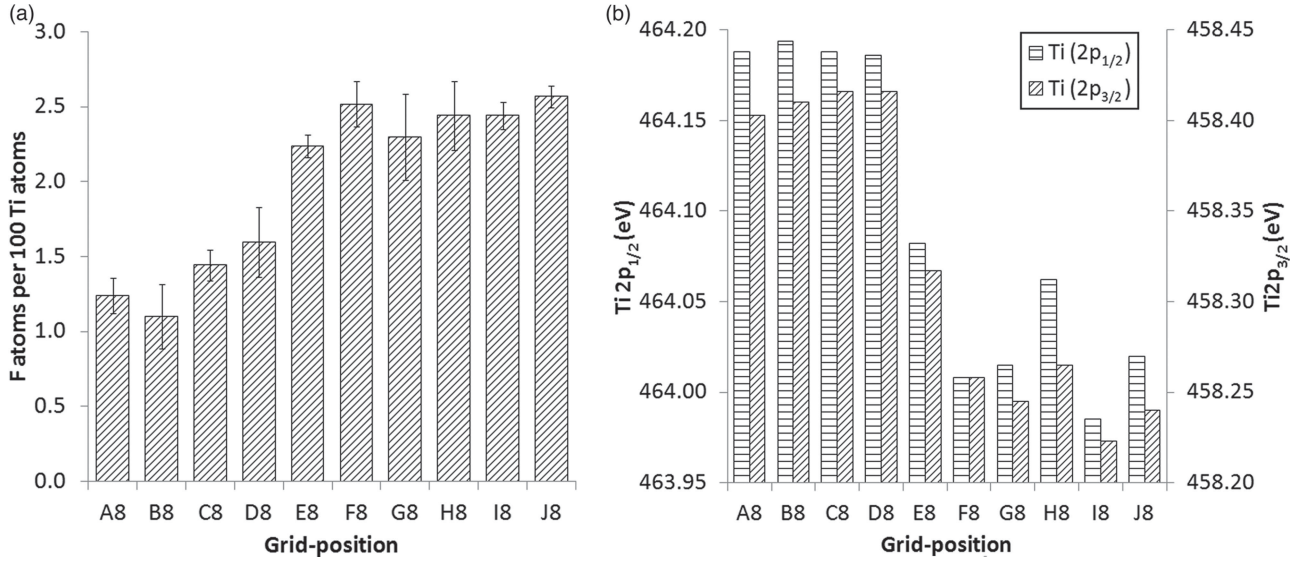

Figure 6. a) The fluorine dopant level (F atoms/100 Ti atoms) and b) the Ti 2p energies determined from the X-ray photoelectron spectroscopy of the 10 grid positions located across Row 8 in the combinatorial F:TiO_2 thin-film.

corresponded to an individual crystal domain. The shape of these crystals changed considerably on moving from the blue region (A8 to D8) to the transparent region (F8 to J8). Within the blue region, crystals were larger and more rounded. Within the transparent region, crystals were smaller, flatter, and more oblong. The crystallites formed at the bridging grid position E8 were more like those formed within the blue region but were partly smaller and more triangular in shape.

2.3.5. UV-Visible Spectroscopy

The UV-visible transmittance and reflectance spectrum (200–2500 nm) was measured for each grid-position across Row 8. The refractive index (n) was determined by the Swanepoel method (Table 1).[45] This allowed film thickness to be re-determined more precisely for each grid position across Row 8 (Table 1). Grid positions within the blue region transmitted near IR light (2500 nm) more weakly (≈3 to 4%) compared with grid positions contained within the transparent region (≈40 to 45%). This weak IR transmittance tailed off into the visible between 750 and 1000 nm (the red region). The preferential absorption of red light may have been the direct cause for the blue color observed. Within the blue region visible light was also more strongly absorbed, where the absorption coefficient was more than double in the blue region (≈4500 cm^{-1}) than in the transparent (≈2000 cm^{-1}) (Table 1). The average level of transmittance in the visible region (400–1000 nm) increased sharply on movement from the blue (≈40%) to the transparent region (≈60%). A red-shift in the band-edge was observed on movement out of the blue region into the transparent (Supporting Information 7(a)) indicating an increase in bandgap energy. The indirect bandgap at each grid-position was determined from a Tauc plot (Supporting Information 7(b))[61]

Grid positions located within the blue region displayed considerably red-shifted bandgaps (≈3.06 eV) relative to un-doped anatase TiO_2 (≈3.20 eV).[62] Movement into the transparent region was accompanied by an increase in bandgap (grid position F8, ≈3.16 eV). Within the transparent region, the bandgap energy increased almost monotonically from ≈3.16 eV at grid position F8 to ≈3.21 eV at grid position J8. All grid-positions (except J8) showed a red-shifted bandgap compared with un-doped TiO_2. Many previous studies on F:TiO_2 have demonstrated red-shifted band-edges, however few have determined the band-gap energy shift. In one study by Todorova et al. a lowered bandgap of 3.07 eV was observed in F:TiO_2 powders (F content ≈ 16 at%) synthesized by a sol-gel route. However, the powders contained a 70:30 mixture of anatase (≈3.2 eV) and rutile (≈3.0 eV) TiO_2 phases. Within N:TiO_2, where nitrogen substitutes oxygen sites, the bandgap decreases linearly with doping level.[40,63–65] Within this F:TiO_2 system, no such relationship was found. In fact, a reverse trend is observed across Row 8, where an increase in the fluorine dopant level resulted in an increased bandgap. This relationship was attributed to a change in dopant site, as indicated by our XPS analysis (Figure 6).

2.3.6. Reaction Chemistry

An anatase TiO_2 thin film with a fluorine doping gradient (F:TiO_2) was synthesized from the combinatorial atmospheric pressure chemical vapor deposition (cAPCVD) of $TiCl_4$, ethyl acetate (EtAc) and trifluoroacetic acid at 500 °C on glass. The film showed no pin-hole defects and no particulates were seen exiting the exhaust, demonstrating the reaction was surface based. Although the APCVD formation of TiO_2 from $TiCl_4$ and H_2O is a lower energy process than the reaction of $TiCl_4$ and EtAc,[66] thin-films formed from the prior reaction are notoriously blotchy and have a tendency to flake. This is because the APCVD reaction of $TiCl_4$ and H_2O to TiO_2 proceeds readily in both the gas phase and at the substrate, whereas the APCVD reaction of $TiCl_4$ and EtAc to TiO_2 proceeds exclusively at the substrate. The exact mechanism by which $TiCl_4$ reacts with EtAc is not known. However, it has been suggested that EtAc decomposes at the surface to produce oxidant species such as ethanol (Equation (4a)), which in turn dehydrates to evolve water and ethane (Equation (4b)). With water present, the surface reaction may then proceed by hydrolysis of $TiCl_4$ (Equation (4c)):[66]

$$CH_3COOC_2H_5 \rightarrow CH_3CH_2OH + C_2H_2O \quad (4a)$$

$$CH_3CH_2OH \rightarrow H_2O + C_2H_4 \quad (4b)$$

$$H_2O + TiCl_4 \rightarrow TiO_2 + 4HCl \quad (4c)$$

The EtAc oxygen source was the limiting reagent in this reaction (**Table 2**). This was fundamental to the quality of the films as higher levels of EtAc can cause carbon contamination.[16] The $TiCl_4$ and EtAc precursors entered the reactor at the same side through entry point A (**Scheme 2**). The thickest point of film growth was not local to their point of entry, indicating the reaction was not mass transport limited. In a typical cold-walled APCVD reaction involving $TiCl_4$ and EtAc, film growth is surface reaction rate limited and most rapid at the centre of the reactor where the substrate is hottest.[39] However, in this system, the most prominent point of film growth was shifted to the left (grid position B6, see Figure 1). We therefore postulate that the introduction of the fluorine precursor inhibited TiO_2 film growth parallel to its point of entry (Scheme 2). The fluorine doping level was greater on its side of entry. This was similar to previous cAPCVD studies of W: TiO_2, where the parallel introduction

Table 2. Reaction conditions in the cAPCVD synthesis of F:TiO_2. The deposition was carried out for 210 s at a reactor temperature of 500 °C under an additional plain line flow of 6 and 3 L min^{-1} through entry points A and B, respectively. EtAc = ethyl acetate, $F_3C_2O_2H$ = trifluoroacetic acid, T = bubbler temperature (°C), F = N_2 carrier gas flow rate (L min^{-1}), Vp = vapor pressure (mmHg) and a = mass flow rate (10^{-3} mol min^{-1}).

	Entry point		
	A		B
	$TiCl_4$	EtAc	$F_3C_2O_2H$
T [°C]	75	33	40
F [L min^{-1}]	1.2	0.25	1.0
Vp [mmHg]	110	136	225
a [10^{-3} mol min^{-1}]	8.3	2.2	17
molar ratio	1.0	0.27	2.1

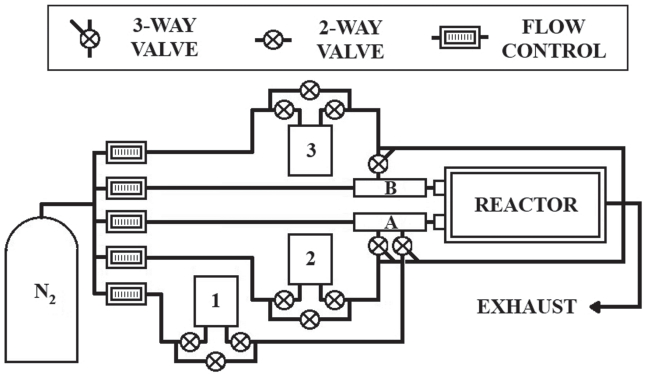

Scheme 2. Schematic of the combinatorial APCVD apparatus used in the synthesis of a F: TiO2 thin-film with graded composition. Bubblers 1, 2, and 3 contained titanium tetrachloride [Ti source], ethyl acetate [O source] and trifluoroacetic acid [F source] precursors, respectively. A and B are neighboring mixing chambers.

of WCl_6 inhibited TiO_2 film growth but led to a higher level of tungsten incorporation.[13] Across Row 8, the F-doping level varied between ≈2.3 and 2.6% (F:Ti) on the right side of the film (grid positions F8–J8) and between ≈1.1 and 1.6% (F:Ti) on the left side of the film (grid positions A8–D8). The overall reaction for the grid positions across Row 8 could be summarized as:

$$TiCl_4 + CH_3COOC_2H_5 + F_3C_2O_2H \rightarrow TiO_{2-x}F_x + \text{by} - \text{products} \quad (5)$$

where $0.011 \leq x \leq 0.026$. Although the level of oxygen precursor (EtAc) introduced into the reaction was almost 8 times lower than the level of fluorine precursor ($F_3C_2O_2H$), the amount of oxygen incorporated was far greater than that of fluorine. If we assume that the oxygen and fluorine present came solely from the EtAc and $F_3C_2O_2H$ precursors respectively, than the EtAc precursor reacted almost 400 times more rapidly than the $F_3C_2O_2H$ precursor.

In the higher doping region, a transparent film was formed with an expanded unit cell, smaller crystallites (≈40–50 nm in diameter) and strong preferred growth in the (112) and (211) crystal planes. In the lower doping region, a blue colored film was formed with a contracted unit cell, larger crystallites (≈90–100 nm in diameter) and strong preferred growth in the (004) and (105) crystal planes. XPS studies indicated that the F-dopants in the blue and transparent region were distinct, yet both of –1 valency. As such, the varied physical changes (i.e., the direction, size and density of crystal growth) were attributed to differences in F-dopant site that had knock-on effects on the functional properties.

2.3.7. Physical-Functional Property Relationships

The electrical properties of the 10 grid positions located across Row 8 were examined in greater depth by the Hall Effect (Table 1). Only grid positions A8 to E8 (positions located within the blue region) possessed resistivities within the detection limits of our device. The resistivities measured by the Hall Effect device were consistently larger than those measured by the four-point probe (Table 1). The number of charge carriers (n) introduced into the system increased from ≈8.4×10^{17} cm^{-3} at grid position A8, maximized at ≈1.2×10^{18} cm^{-3} at grid position D8 and then fell sharply to a minimum of ≈3.7×10^{17} cm^{-3} at grid position E8. Conversely, the electron mobility (μ) increased sharply from ≈20 to 30 cm^2 V^{-1} s^{-1} for grid positions A8 to D8 (positions completely within the blue patch) to ≈70 cm^2 V^{-1} s^{-1} at grid position E8 (located at the edge of the blue patch). As grid position E8 represented an intermediate state between blue and transparent F:TiO_2, this indicated electron mobility would increase into the transparent region (grid positions F8 to J8). As the resistivities were close to the lower limits that can be measured by the Hall Effect device, the derived charge carrier densities and mobilities were liable to have large associated errors. As such, the quoted values are merely indicative. Temperature dependent Hall Effect measurements were carried out on grid-position C9 under liquid nitrogen (–196 °C), within an acetone dry-ice bath (–78 °C) and again in air (25 °C) (**Table 3**). A relationship akin to an extrinsic semiconductor was observed, with electrical conduction decreasing only marginally and charge carrier concentrations remaining high (within the 5×10^{18}–5×10^{19} cm^{-3} range). Electron mobilities (0.50–2.0 cm^2 V^{-1} s^{-1}) varied less significantly than charge carrier concentration, which indicated grain boundary scattering was the more dominant process. A significant increase in charge carrier concentration (more than an order of magnitude) was observed at grid position C9 (n = -4.4×10^{19} cm^{-3}) relative to its neighboring grid position C8 (n = -9.4×10^{17} cm^{-3}). However, electron mobility was substantially lower (μ = 0.50 versus 29 cm^2 V^{-1} s^{-1}). Overall, electrical conductivity was lower at grid position C9 than at C8 (0.28 versus 0.23 Ω cm), where the discrepancies in Hall Effect components may have been exacerbated by being at the limits of the device.

The carrier mobilities observed in this F:TiO_2 system surpassed those observed by Mohri et al. in their most electrically conductive F:TiO_2 film synthesized by PLD (μ < 10 cm^2 V^{-1} s^{-1}).[15] However, their film was far less resistive (ρ = 1.6×10^{-3} Ω cm) than any material analyzed in this study primarily because of the superior level of charge carriers introduced (n = 1.6×10^{21} cm^{-3}). This was achieved at a F-doping level of 5% (F:Ti). Comparing the two studies we find that the charge carrier level was not linearly dependent on the doping level. We attribute this to the ultra-high vacuum condition in which their F:TiO_2 was formed, which typically leads to films of higher purity and a reduced number of defects. The high level of charge carriers achievable in F:TiO_2 was similar to that in optimized metal-ion doped systems such as Nb (n = 2.0×10^{21} cm^{-3})[18] and Ta (n = 1.4×10^{21} cm^{-3}).[19] However, the mobility of these carriers were comparatively hindered compared with Nb:TiO_2

Table 3. Temperature dependent Hall Effect components measured at grid position C9.

T (°C)	Resistivity [Ω cm]	n [$\times 10^{18}$ cm^{-3}]	μ [cm^2 V^{-1} s^{-1}]
–196	0.57	–5.3	2.1
–78	0.58	–8.3	1.3
25	0.28	–44	0.50

($\mu \approx 70$ cm^2 V^{-1} s^{-1}) and Ta:TiO_2 ($\mu \approx 30$ cm^2 V^{-1} s^{-1}), and more akin to carriers found in W:TiO_2 (<10 cm^2 V^{-1} s^{-1}),[14] which resulted in a poorer overall conductivity.

The photocatalytic activity within the transparent region (FQY $\approx$ 12–20 $\times$ 10^{-5}) was up to twice as efficient as those observed in the blue region (FQY $\approx$ 7–11 $\times$ 10^{-5}). However, these activities were significantly lower than those observed in analogous photocatalytic studies of pure phase anatase TiO_2 formed similarly by APCVD (FQY $\approx$ 2.5 $\times$ 10^{-3}).[41] This may have been due to the restricted growth in both the (101) and (004) planes in both materials, where it has been shown that optimal photocatalytic activity in TiO_2 nanocrystals is found when the growth of these planes are equally promoted.[67,68] A greater detriment to both the FQE and FQY of photocatalysis was observed in blue F:TiO_2. This was attributed to the more inhibited movement of photo-generated charge carriers in blue F:TiO_2 as opposed to transparent F:TiO_2. For these reasons, thinner regions of film displayed an enhanced FQY as photogenerated charge carriers were more likely to reach the surface and take part in photocatalysis (Figure 3).

2.3.8. Computational Analysis of Fluorine Impurities

A plot of formation energy as a function of Fermi-level position for F_O (where F atoms replace O sites) and F_i (where F atoms sit at interstitial sites) impurities for both Ti-rich/O-poor and Ti-poor/O-rich growth regimes is displayed in **Figure 7**. F_O behaves as a shallow donor in both growth regimes and is stable only in the +1 charge state across the entire bandgap. This is consistent with the high levels of conductivity present in this study and reported elsewhere.[69] The F_i site is an amphoteric defect in anatase TiO_2. It exists in all three charge states in the bandgap, acting as an acceptor when the Fermi level is near the conduction band minimum (CBM) and as a donor when then Fermi level is near the valence band maximum (VBM). At the idealized oxygen-rich limit, the F_i^{-1} starts to compensate electrons from the F_O site when the Fermi level is just below the CBM. In our synthesis, film growth did not occur in an O-rich environment. Therefore, the formation energy of F_O will decrease towards the O-poor value. Similarly the formation energy for F_i will increase towards the O-poor value and the intersection of these lines (the point at which F_i^{-1} starts to compensate F_O) will move into the conduction band. Therefore, at low doping concentrations, F impurities first occupy an oxygen lattice site (F_O). Such F-doping was present in our combinatorial system within the highly conductive blue region (grid positions A8 to D8). When the doping concentration reaches a critical percentage, F_i^{-1} starts to dominate and kill free-electrons in this system. Such F-doping was present in our combinatorial system within the poorly conductive transparent region (grid-positions H8 to J8). This explains the observed drop in conductivity as the doping level increases beyond a critical value (found experimentally to lie beyond a doping level of ≈2.3% F:Ti). Computation showed that the core level for F_i lies 1.17 eV closer to the VBM than F_O. This was in line with XPS evidence that showed a small shift in the binding energy of the F 1s environment on movement from the blue (684.8 eV) to transparent region (684.5 eV). This shift was therefore representative of an average change in binding energy as F_i^{-1} dopants began to form within the F_O doped lattice

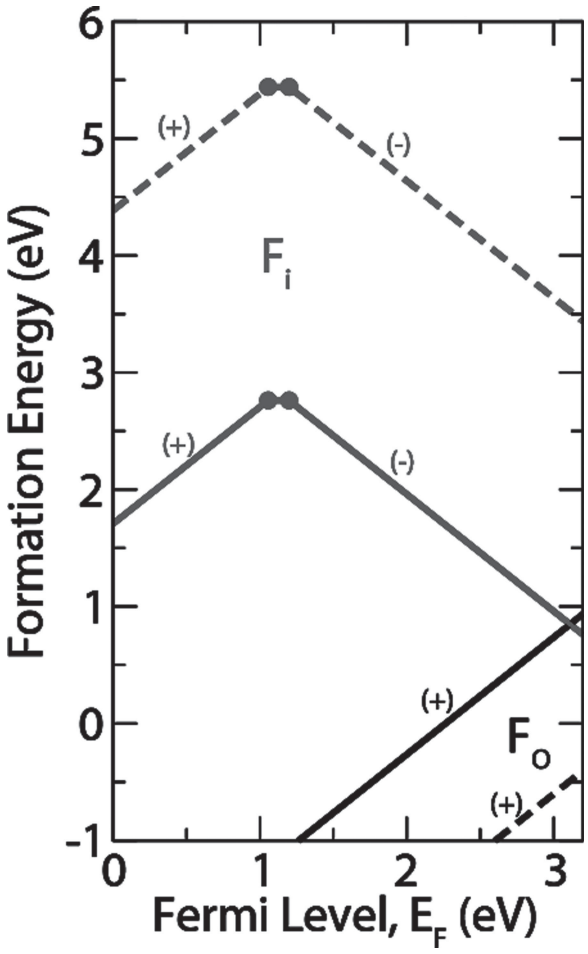

Figure 7. HSE06 calculated formation energies of F impurities in anatase TiO_2. The solid lines indicate Ti-poor/O-rich conditions, and the dashed lines indicate Ti-rich/O-poor conditions. The solid dots represent the transition levels, $\varepsilon(q'/q)$.

at higher F concentrations. This was in agreement with the studies of Di Valentin et al. who also observed two distinct F^- doping sites that also differed in energy by ≈1.2 eV.[60]

Figure 8 displays the electronic structure of these defects. Figure 8(a) illustrates that excess electrons from F_O dopants are donated directly into the conduction band (degenerate semiconductor) and is further evidence of F_O formation in the blue region. Figure 8(b) shows that F_i dopants possess a deep acceptor level ≈2.8 eV above the VBM caused by a hole centered primarily on the F impurity. This type of F-doping could explain the phenomenon of visible light photocatalysis in some F-doped TiO_2 samples[20–28] through a multi-photon excitation process. Figure 8(c) shows how F_i^{-1} dopants do not possess a defect state in the band gap as excess electrons fill the unoccupied acceptor level from *Fi*. In the transparent region of our film poor electrical conductivity was observed. XPS analysis signified the presence of F anions in the −1 charge state and visible light photocatalysis was not observed. These evidences signified the presence of F_i^{-1} formation in the transparent region. The UVA photocatalysis doubled when moving from the blue to transparent region. This was attributed to a change in dominance

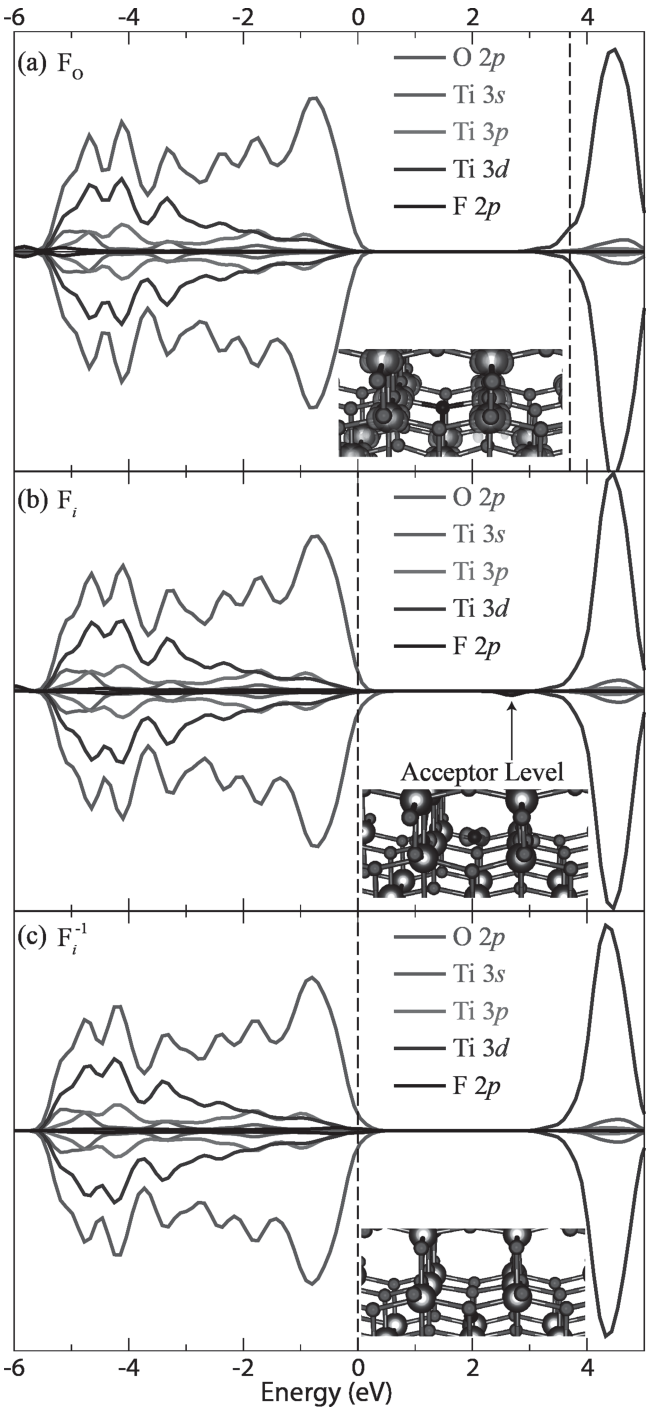

Figure 8. Partial energy density of states (PEDOS) for a) F_O, b) F_i, and c) F_i^{-1} in the 108 atom anatase TiO_2 supercell. The highest occupied state is indicated by the vertical dashed line in each case. The three PEDOS are aligned (set to 0 eV) relative to the highest occupied point in the valence band. The density of states included a Gaussian smearing of 0.2 eV.

of F-dopant (from F_O to F_i^{-1}) and rationalized in terms of increased electron mobility. Although electrical conduction in the transparent region was too low for electron mobility to be measured (grid positions F8–J8), an intermediate point at grid position E8 possessed an electron mobility more than double

Table 4. HSE06 calculated relaxed volumes for defects in the anatase TiO_2.

Cell	Volume [Å^3]
Pure	137.84
F_O	138.17
F*i*	138.42
Fi^{-1}	139.16

that of any other measured point (Table 1). This indicated electron mobility would increase with further movement into the transparent region. Although increased F_i^{-1} doping killed free-electron carriers (*n*), the higher electron mobilities contained in this region would have better allowed free movement of photo-generated electron-hole pairs that facilitate photocatalysis. This case is analogous to N: TiO_2, where nitrogen dopants that replace oxygen sites (N_O) inject free-electron carriers but severely hinder electron mobility and nitrogen dopants that move into interstitial sites (N_i) do not inject free-electron carriers but do not hinder electron mobility.[40,70,71] Interestingly, when electrically neutral F_i dopants enter the lattice an acceptor level is observed in the DOS; analogous to N_i dopants.[70]

The large volume increase observed experimentally upon surpassing a critical fluorine doping level was observed computationally as well. In **Table 4** we show the volumes for the pure and defective supercells which have been allowed to relax after incorporating the F impurity. Although the F_O causes a small expansion of the lattice, the formation of F_i^{-1} causes a much greater expansion; consistent with the X-ray crystallography (Table 1).

At the end of the introduction section three questions were posed in relation to this F:TiO_2 system asking: (i) why a blue region forms (ii) why electrical conduction is greater in the blue region, and (iii) why photocatalysis is lower in the blue region. In relation to why a blue colored material is formed we found that the substitutional F_O doping primarily found in this region forms a degenerate semiconductor with a significant level of charge carriers ($\approx 1 \times 10^{18}$ cm^{-3}) that absorb strongly in the late visible-NIR region (i.e., red light) thus making the material appear blue. Electrical conduction in the blue region was greater as F_O fluorine dopants acted as shallow donors whereas F_i^{-1} dopants, which become dominant in the transparent region, killed free-electron donation. It was postulated that lower levels of photocatalysis were present in the blue region due to the inhibited movement of photo-generated charge carriers (i.e., due to restricted electron mobility). Although our findings wholly support the answers to the first two questions posed, the observed trends in photocatalysis could also be attributed to differences in preferred crystal growth and the number of active surface sites that facilitate photocatalysis.

Within this combinatorial system, a trade-off between low electrical resistance and high UVA photocatalytic activity was present with either F_O doping (blue region) or F_i^{-1} doping (transparent region). Experimentally, a high growth rate/substrate temperature and a lower F-doping level favored F_O doping. Insights from our computational analysis (Figure 7),

indicates that a higher level of F_O doping can be achieved in F:TiO_2 before F_i^{-1} doping predominates if grown in more Ti-rich/O-poor conditions. In such a case, a more conductive material should form due to the injection of free charge carriers. Such an improved material might be achieved through APCVD by increasing the F/Ti and Ti/O precursor ratios. Visible transparency could be improved by decreasing film thickness (i.e., simply decreasing the deposition time), whilst maintaining the aesthetic blue-tinge. Although the best TiO_2-TCOs produced by physical deposition methods are up to 10^3 times more conductive than the most conductive material reported herein,[72] achieving a low resistance TiO_2-based TCO by a low cost and up-scalable method such as APCVD is essential if this is to become a marketable product. Improving the photocatalytic activity of blue F:TiO_2 remains a significant challenge as electron mobility decreases at the expense of increases in free charge carriers. We thus postulate that an increased active surface area might circumvent the reduction in photocatalytic activity at the cost of increased haze and transparency losses, opening up applications as robust TCO layers with the added benefit of a self-cleaning function. The color and high IR reflectivity also makes this material a desirable candidate for aesthetic blue-colored solar control glazing.

3. Conclusions

An anatase TiO_2 thin film with a graded level of fluorine dopant (F:TiO_2) was formed from a combinatorial atmospheric pressure chemical vapor deposition (cAPCVD) on glass from the reaction of titanium tetrachloride with ethyl acetate and trifluoroacetic acid at 500 °C. The photocatalytic activity and electrical resistivity of 200 allotted positions across a grid (10 × 20; columns × rows) were screened using high-throughput methods. A blue region of film was singled out for containing the lowest electrical resistivities of any TiO_2-based system formed by APCVD before ($\rho \approx 0.22$–$0.45\ \Omega$ cm, $n = 8.4$–12.4×10^{17} cm^{-3}, $\mu = 18$–33 $cm^2\ V^{-1}s^{-1}$).

The blue region contained a lower fluorine doping level (F:Ti ≈ 1.1–1.6%) than its neighboring transparent region (F:Ti ≈ 2.5%). Substantial changes in unit cell volume, preferred crystal growth and size, Ti 2p and F 1s binding energy and bandgap energy were seen above a critical doping level (F:Ti ≥ 2.3%), indicating the presence of two unique fluorine dopant sites. The two types of F-dopant were identified by ab initio calculations alongside experiment to be:

- F_O dopants that replace oxygen sites, observed below the critical doping level (blue F:TiO_2), which introduce electron charge carriers more freely ($n = 8$–12×10^{17} cm^{-3})
- F_i^{-1} dopants that sit at interstitial sites, observed above the critical doping level (transparent F:TiO_2), which kill free-electron donation and causes the lattice to expand significantly (by up to 2.4% against pure TiO_2)

By using the combinatorial approach, a composition was found between the transparent and colored regions that simultaneously acted as a photocatalyst and transparent conducting oxide. Analyzing combinatorial systems in conjunction with high-throughput screening tools and cutting edge computational defect chemistry analysis provides a shortcut to understanding physical-functional property relationships in great depth and offers a rapid method for discovering optimum compositions and new materials.

4. Experimental Section

All chemicals were purchased from Sigma-Aldrich Chemical Co; resazurin 92%, hydroxyethyl cellulose (HEC) [average $M_v \approx 90\ 000$], glycerol 99.5%, isopropanol 99.98%, acetone 99%, ethyl acetate (EtAc) 99%, titanium chloride ($TiCl_4$) 99.9%, and trifluoroacetic acid ($F_3C_2O_2H$) 99%. Di-nitrogen gas cylinders were supplied by BOC. The glass substrate, consisting of a standard piece of 3.2 mm thick float glass coated with a 50 nm silica (SiO_2) barrier layer was supplied by the Pilkington NSG Group.

Combinatorial Film Synthesis: An anatase TiO_2 thin-film with a fluorine doping gradient (F:TiO_2) was grown by combinatorial atmospheric pressure chemical vapor deposition (cAPCVD). This involved the reaction of $TiCl_4$ [Ti source] with ethyl acetate [O source] and trifluoroacetic acid [F source] at 500 °C. The film was grown on standard float glass of dimensions 90 mm × 225 mm × 3.2 mm (length × breadth × thickness) inside a cold-walled reactor heated on its underside using a graphite block. The substrate was coated with a SiO_2 barrier layer that prevented the migration of ions from within the glass into the film. A schematic of the cAPCVD apparatus is shown in Scheme 2.

The reagents were volatilized in heated bubblers and then transported to their respective mixing chamber by an inert N_2 carrier gas. $TiCl_4$ and EtAc were carried from bubblers 1 and 2, respectively, to mixing chamber A, where the gas streams were combined. $F_3C_2O_2H$ was transported from bubbler 3 to mixing chamber B. Additional plain flows of N_2 gas introduced the precursors from their mixing chambers through a baffle manifold and into the reactor. The Ti and O sources entered the reactor at the same inlet and the F source was introduced through an adjacent inlet. This created a horizontal gradient in the F:Ti precursor ratios and the range of deposition conditions required for the combinatorial aspect of this work. The heat gradient experienced within cold-walled reactors from heat dissipation (±15–20 °C) coupled with the asymmetric introduction of the precursors that formed TiO_2 caused a film with a thickness gradient to be formed. The parameters used to deposit the combinatorial film are shown in Table 2. The carbon heating block was maintained at 500 °C during the 210 s deposition. Mass flow rates (10^{-3} mol min^{-1}) were derived from vapor pressure (mm Hg) curves yielding molar ratios of each precursor (normalized to $TiCl_4$ at 1.0).[73]

Screening Methods: Film-thickness was determined using a Filmetrics F20 instrument. Optical reflectance spectra were recorded over the 300–1000 nm range using a fiber optic detector (<3 s) and used to determine film thickness with derivations based on the Swanepoel method[45] by automated software. The refractive index of a TiO_2 standard was used in each calculation.

The sheet resistance was measured using a fixed-width spring-mounted four-point electrode (≈1 cm wide). A constant voltage was applied using a Maplin N93CX switching mode power supply. Voltages and currents were measured using a Caltek CM2700 and a Sinometer M-830B meter diode respectively. The electrode was placed at the heart of each position analyzed. As each grid position was spaced 0.75 cm apart this meant there was 0.25 cm over-spill onto neighboring sites.

The photocatalytic activity was assessed using a screening method employing dye degradation that relies on digital photography to monitor the reaction progression.[46,47] A resazurin-based intelligent ink was the test organic.[48] The ink consisted of resazurin (40 mg) redox dye in an aqueous solution (40 mL) with glycerol (3 g) and hydroxylethyl cellulose (0.45 g) that was aged for a day before use. The F:TiO_2

film was first washed with distilled water, rinsed with isopropanol and then placed under UVC irradiation (254 nm, 2 × 8 W – Vilber Lourmat VL-208G) for 1 hr to ensure the surface was free from contaminants. An even layer of ink was applied onto wall-mounted combinatorial films using an aerosol-spray gun (SIP Emerald Spray Gun/Halfords Plc) at an air-pressure feed of 3.5 bar. A blank microscope slide (VWR ISO 8037/1, 76 × 26 mm) was coated simultaneously in order to assess the thickness of the ink-coating by UV-visible spectroscopy (PerkinElmer Lambda 25 UV/VIS spectrometer). Photocatalysis was instigated using UVA irradiation (365 nm, 2 × 8 W – Vilber Lourmat VL-208BL) and monitored by digital photography (Epson Perfection 1200 Photo Scanner). The red–green–blue components of color were extracted from each digital image using RGB Extractor.[49] The time taken for the red component of digital color to plateau at each grid-position was determined by fitting the color data to a Boltzmann model using Origin 8.0.[50]

Physical Characterization: X-ray crystallography was carried out using a micro-focus Bruker GADDS powder X-ray diffractometer, with a monochromated Cu K (1.5406 Å) source and a CCD area X-ray detector, capable of 0.01° resolution in 2θ with an automated X–Y movable stage. Patterns were fit to a Le Bail refined model using the GSAS-EXPGUI software suite.[74] Raman spectroscopy was conducted using a Renishaw 1000 Raman spectrometer equipped with a red laser (633 nm) over the 100–1000 cm^{-1} energy range. X-ray photoelectron spectroscopy (XPS) was carried out using a Thermo K-Alpha spectrometer using monochromated Al K radiation. Survey scans were collected over the 0–1400 eV binding energy range with 1 eV resolution and a pass energy of 200 eV. Higher resolution scans (0.1 eV) encompassing the principal peaks of Ti (2p), O (1s), F (1s), C (1s) and Si (2p) were also collected at a pass energy of 50 eV. An Ar-ion gun was used to etch the surface layers of samples to record a depth profile. A sputtering time of 5 s per level was used. The survey and high resolution scans were collected once again between each sputter cycle for a total of 4 levels. Peaks were modeled using CasaXPS.[75] Peak positions were adjusted to adventitious graphite (284.5 eV) and areas were converted using the appropriate sensitivity factors[76] to determine the concentration of each state. The average concentration relative to total titanium at the four depths was taken as the fluorine doping level, with the standard deviation taken as the error. The surface microstructure was investigated by scanning electron microscopy (SEM) using a JOEL-6301F field emission instrument. Transmittance and reflectance spectra were recorded over the 200–2500 nm range using a Helios double beam instrument. Room temperature Hall effect measurements were carried out on an Ecopia HMS-3000 in the Van der Pauw configuration.[51] Measurements were acquired at 0.58 T and a current of 0.1 μA on square-cut samples (≈0.75 × 0.75 cm). Silver paint (Agar Scientific) was used to form ohmic contacts, the integrity of which were tested prior to measurement.

Theoretical Methods: Calculations were performed using the VASP[77] code, with the projector augmented wave approach[78] used to describe the interaction between the core (Ti:[Ar], F:[Kr], and O:[He]) and valence electrons. The calculations were performed using the screened hybrid functional as proposed by Heyd, Scuseria, and Ernzerhof[79] in which a percentage of exact nonlocal Fock exchange is added to the Perdew, Purke and Ernzerhof[80] functional with a screening of $\omega = 0.11$ $bohr^{-1}$ applied to partition the Coulomb potential into long range and short range terms. The HSE06 approach consistently produces structural and band gap data that are more accurate than standard density functional approaches, such as the local density approximation (LDA) or the generalized gradient approximation (GGA).[81–84] A cut-off of 500 eV and a k-point mesh of 6 × 6 × 2, centred on the Γ point were found to be sufficient. All calculations were deemed to be converged when the forces on all atoms were less than 0.01 $eV.Å^{-1}$.

Two doping mechanisms, fluorine replacing a lattice oxygen (F_O) and fluorine on an interstitial site (F_i) were tested in a 108 atom (3 × 3 × 1) supercell, with a k-point mesh of Γ-centred 2 × 2 × 2. The formation energy of a defect determines its equilibrium concentration. For defect D in charge state q, the formation energy is given by

$$\Delta H_f(D \cdot q) = \left(E^{D \cdot q} - E^H\right) + \sum_i n_i \left(E_i + \mu_i\right) + \left(E_{Fermi} + \varepsilon^H_{VBM}\right) + E_{align}[q] \quad (6)$$

where E^H is the energy of the pure host supercell, and $E^{D,\,q}$ is the energy of the defective cell.[85–87] E_i corresponds to elemental reference energies, i.e., Ti(s), O_2(g), and F_2(g) energies, μ_i is the chemical potential of the species in question and n is the number of atoms added to or taken from an external reservoir. Electrons are exchanged with the Fermi level (E_F), which ranges from the VBM (E_F = 0 eV) to the CBM. $\varepsilon_{VBM}{}^H$ is the VBM eigenvalue of the host bulk and $E_{align}[q]$ is a correction used to align the VBM of the bulk and the defective supercells and also to correct for finite-size effects in the calculations of charged defects, performed using the freely available SXDEFECTALIGN code.[88] These finite-size effect corrections are necessary as the charge introduced into a cell can cause a spurious interaction with its periodic image, which can affect the energetics.[88,89] A correction for band filling by defect levels resonant in the conduction band was also included.[90]

The chemical potentials, μ_i, reflect the specific equilibrium growth conditions, within the global constraint of the calculated enthalpy of the host, in this case TiO_2: μTi + 2μO = $\Delta Hf(TiO_2)$. The lower limit for μO, which characterizes a Ti-rich/O-poor environment, is determined by the formation of Ti_2O_3: $\Delta\mu Ti = [2\Delta H_f(TiO_2) - \Delta H_f(Ti_2O_3)]$; $\Delta\mu O = [2\Delta H_f(Ti_2O_3) - 3\Delta H_f(TiO_2)]$. The upper limit for μO (Ti-poor/O-rich conditions) is governed by O_2 formation. The F chemical potential was defined with respect to the formation energy of TiF_3.

The thermodynamic transition levels (ionization levels) of a given defect, $\varepsilon_D(q/q')$, correspond to the Fermi-level positions at which a given defect changes from charge state q to q′.

$$\varepsilon_D\left(\frac{q'}{q}\right) = \frac{\Delta H^f(D,q) - \Delta H^f(D,q')}{q' - q} \quad (7)$$

The HSE06 calculated a and c lattice parameters for anatase TiO_2 are 3.784 Å and 9.626 Å respecitively, which are in very good agreement with the experimental lattice parameters of 3.784 Å and 9.512 Å respectively.[91] The HSE06 calculated indirect band gap is 3.28 eV, in good agreement with recent HSE06 studies of anatase TiO_2.[92] Importantly, HSE06 has been shown to provide a correct description of related degenerate TCO Nb-doped anatase,[93,94] whereas as the DFT+U functional[95] and other hybrid DFT functionals[69] have qualitatively failed to reproduce the degenerate semiconducting nature. The HSE06 approach also fulfils the "generalized Koopmans theorem"[96] for acceptor and donor defects in anatase TiO_2,[93] which makes it the obvious choice to study defects in F-doped TiO_2.

Supporting Information

Supporting Information is available from the Wiley Online Library or from the author.

Acknowledgements

The authors would like to thank the EPSRC for funding (platform grant EP/H00064X). A.K and D.O.S. are grateful to the Ramsay Memorial Trust, University College London and Imperial College London for the provision of their Ramsay Fellowships. The work presented here made use of the UCL Legion HPC Facility, the IRIDIS cluster provided by the EPSRC funded Centre for Innovation (EP/K000144/1 and EP/K000136/1), and the HECToR supercomputer through membership of the UK's HPC Materials Chemistry Consortium, which is funded by EPSRC Grant No. EP/F067496.

Received: April 19, 2013
Revised: June 25, 2013
Published online: November 19, 2013

[1] A. Mills, S. Le Hunte, *J. Photochem. Photobiol., A* **1997**, *108*, 1.
[2] A. Fujishima, X. Zhang, D. Tryk, *Surf. Sci. Rep.* **2008**, *63*, 515.
[3] E. Selli, G. L. Chiarello, E. Quartarone, P. Mustarelli, I. Rossetti, L. Forni, *Chem. Commun.* **2007**, 5022.
[4] A. Mills, M. Valenzuela, *J. Photochem. Photobiol., A* **2004**, *165*, 25.
[5] F. E. Osterloh, *Chem. Mater.* **2008**, *20*, 35.
[6] N. Savage, *Sens. Actuators, B* **2001**, *79*, 17.
[7] K. Hashimoto, H. Irie, A. Fujishima, *Jpn. J. Appl. Phys.* **2005**, *44*, 8269.
[8] C. W. Dunnill, Z. A. Aiken, J. Pratten, M. Wilson, D. J. Morgan, I. P. Parkin, *J. Photochem. Photobiol., A* **2009**, *207*, 244.
[9] K. Page, R. G. Palgrave, I. P. Parkin, M. Wilson, S. L. P. Savin, A. V. Chadwick, *J. Mater. Chem.* **2007**, *17*, 95.
[10] A. Rampaul, I. P. Parkin, S. A. O'Neill, J. Desouza, A. Mills, N. Elliott, *Polyhedron* **2003**, *22*, 35.
[11] C. W. Dunnill, Z. A. Aiken, A. Kafizas, J. Pratten, M. Wilson, D. J. Morgan, I. P. Parkin, *J. Mater. Chem.* **2009**, *19*, 8747.
[12] A. Kafizas, S. Kellici, J. A. Darr, I. P. Parkin, *J. Photochem. Photobiol., A* **2009**, *204*, 183.
[13] A. Kafizas, I. P. Parkin, *J. Am. Chem. Soc.* **2011**, *133*, 20458.
[14] U. Takeuchi, A. Chikamatsu, T. Hitosugi, H. Kumigashira, M. Oshima, Y. Hirose, T. Shimada, T. Hasegawa, *J. Appl. Phys.* **2010**, *107*, 023705.
[15] S. Mohri, Y. Hirose, S. Nakao, N. Yamada, T. Shimada, T. Hasegawa, *J. Appl. Phys.* **2012**, *111*, 093528.
[16] A. Kafizas, C. W. Dunnill, I. P. Parkin, *J. Mater. Chem.* **2010**, *20*, 8336.
[17] A. Kafizas, I. P. Parkin, *J. Mater. Chem.* **2010**, *20*, 2157.
[18] Y. Furubayashi, T. Hitosugi, Y. Yamamoto, K. Inaba, G. Kinoda, Y. Hirose, T. Shimada, T. Hasegawa, *Appl. Phys. Lett.* **2005**, *86*, 252101.
[19] T. Hitosugi, Y. Furubayashi, A. Ueda, K. Itabashi, K. Inaba, Y. Hirose, G. Kinoda, Y. Yamamoto, T. Shimada, T. Hasegawa, *Jpn. J. Appl. Phys.* **2005**, *44*, L1063.
[20] N. Todorova, T. Giannakopoulou, G. Romanos, T. Vaimakis, J. Yu, C. Trapalis, *Int. J. Photoenergy* **2008**, *2008*, 1.
[21] D. Li, H. Haneda, S. Hishita, N. Ohashi, N. K. Labhsetwar, *J. Fluorine Chem.* **2005**, *126*, 69.
[22] D. Li, H. Haneda, N. K. Labhsetwar, S. Hishita, N. Ohashi, *Chem. Phys. Lett.* **2005**, *401*, 579.
[23] Y.-L. Su, Y. Li, Y.-X. Du, L.-C. Lei, *Acta Phys.-Chim. Sin.* **2011**, *27*, 939.
[24] Y. Yu, H.-H. Wu, B.-L. Zhu, S.-R. Wang, W.-P. Huang, S.-H. Wu, S.-M. Zhang, *Catal. Lett.* **2007**, *121*, 165.
[25] A. Hattori, H. Tada, *J. Sol-Gel Sci. Technol.* **2001**, *4*, 47.
[26] G. Wu, A. Chen, *J. Photochem. Photobiol., A* **2008**, *195*, 47.
[27] J. Xu, Y. Ao, D. Fu, C. Yuan, *Appl. Surf. Sci.* **2008**, *254*, 3033.
[28] S. Yan, T. Sun, *Adv. Mat. Res.* **2011**, *299-300*, 171.
[29] L. Di, N. Ohashi, S. Hishita, T. Kolodiazhnyi, H. Haneda, *J. Solid State Chem.* **2005**, *178*, 3293.
[30] Y. Zhao, X. Du, X. Wang, J. He, Y. Yu, H. He, *Sens. Actuators, B* **2010**, *151*, 205.
[31] T. Giannakopoulou, N. Todorova, C. Trapalis, T. Vaimakis, *Mater. Lett.* **2007**, *61*, 4474.
[32] T. Yamaki, T. Umebayashi, T. Sumita, S. Yamamoto, M. Maekawa, A. Kawasuso, H. Itoh, *Nucl. Instrum. Methods Phys. Res., Sect. B* **2003**, *206*, 254.
[33] T. Yamaki, T. Sumita, S. Yamamoto, *J. Mater. Sci. Lett.* **2002**, *21*, 33.
[34] H. T. Eun, Y. S. Ko, *J. Ind. Eng. Chem.* **2003**, *9*, 348.
[35] M. Ait Aouaj, R. Diaz, A. Belayachi, F. Rueda, M. Abd-Lefdil, *Mater. Res. Bull.* **2009**, *44*, 1458.
[36] R. Diaz, H. Bihri, M. Ait Aouaj, F. Rueda, *Eur. Phys. J.-Appl. Phys.* **2007**, *38*, 217.
[37] S. A. O'Neill, R. J. H. Clark, I. P. Parkin, N. Elliott, A. Mills, *Chem. Mater.* **2003**, *15*, 46.
[38] A. Kafizas, C. W. Dunnill, G. Hyett, I. P. Parkin, *ECS Trans.* **2010**, *25*, 139.
[39] G. Hyett, M. Green, I. P. Parkin, *J. Am. Chem. Soc.* **2006**, *128*, 12147.
[40] A. Kafizas, C. Crick, I. P. Parkin, *J. Photochem. Photobiol., A* **2010**, *216*, 156.
[41] A. Kafizas, C. J. Carmalt, I. P. Parkin, *Chem. Eur. J.* **2012**, *18*, 13048.
[42] G. Hyett, I. P. Parkin, *Surf. Coat. Technol.* **2007**, *201*, 8966.
[43] A. Kafizas, G. Hyett, I. P. Parkin, *J. Mater. Chem.* **2009**, *19*, 1399.
[44] S. Tanemura, L. Miao, P. Jin, K. Kaneko, A. Terai, N. Nabatova-Gabain, *Appl. Surf. Sci.* **2003**, *212*, 654.
[45] R. J. Swanepoel, *J. Phys. E* **1983**, *16*, 1214.
[46] A. Kafizas, A. Mills, I. P. Parkin, *Anal. Chim. Acta* **2010**, *663*, 69.
[47] A. Kafizas, D. Adriaens, A. Mills, I. P. Parkin, *Phys. Chem. Chem. Phys.* **2009**, *11*, 8367.
[48] A. Mills, J. Wang, S.-K. Lee, M. Simonsen, *Chem. Commun.* **2005**, *21*, 2721.
[49] RGB Extractor. http://www.ucl.ac.uk/chemistry/staff/academic_pages/ivan_parkin/research, accessed: October, 2013.
[50] OriginLab, Origin 8.0. http://www.originlab.com/, accessed: October, 2013.
[51] L. J. van der Pauw, *Philips Res. Rep.* **1958**, *13*, 1.
[52] A. Patterson, *Phys. Rev.* **1939**, *56*, 978.
[53] S. Rigby, A. Alobaidi, S. Lee, D. Mcstay, P. Robertson, *Appl. Surf. Sci.* **2006**, *252*, 7948.
[54] T. Ohsaka, F. Izumi, Y. Fujiki, *J. Raman Spectrosc.* **1978**, *7*, 321.
[55] D.-S. Kim, J.-H. Yang, S. Balaji, H.-J. Cho, M.-K. Kim, D.-U. Kang, Y. Djaoued, Y.-U. Kwon, *Cryst. Eng. Commun.* **2009**, *11*, 1621.
[56] C. J. Powell, A. Jablonski, I. S. Tilinin, S. Tanuma, D. R. Penn, *J. Electron. Spectrosc. Relat. Phenom.* **1999**, *98–99*, 1.
[57] V. M. Khomenko, K. Langer, H. Rager, A. Fett, *Phys. Chem. Miner.* **1998**, *25*, 338.
[58] J. C. Yu, *Chem. Mater.* **2002**, *14*, 3808.
[59] D.-G. Huang, S.-J. Liao, J.-M. Liu, Z. Dang, L. Petrik, *J. Photochem. Photobiol., A* **2006**, *184*, 282.
[60] A. M. Czoska, S. Livraghi, M. Chiesa, E. Giamello, S. Agnoli, G. Granozzi, E. Finazzi, C. Di Valentin, G. Pacchioni, *J. Phys. Chem. C* **2008**, *112*, 8951.
[61] J. Tauc, *Mater. Res. Bull.* **1968**, *3*, 37.
[62] D. O. Scanlon, C. W. Dunnill, J. Buckeridge, S. A. Shevlin, A. J. Logsdail, S. M. Woodley, C. R. A. Catlow, M. J. Powell, R. G. Palgrave, I. P. Parkin, G. W. Watson, T. W. Keal, P. Sherwood, A. Walsh, A. A. Sokol, *Nat. Mater.* **2013**, *12*, 798.
[63] X. Jiang, Y. Wang, C. Pan, *J. Am. Ceram. Soc.* **2011**, 1.
[64] L. Zhao, Q. Jiang, J. Lian, *Appl. Surf. Sci.* **2008**, *254*, 4620.
[65] P.-G. Wu, C.-H. Ma, J. K. Shang, *Appl. Phys. A* **2004**, *81*, 1411.
[66] P. Evans, M. E. Pemble, D. W. Sheel, *Chem. Mater.* **2006**, *18*, 5750.
[67] N. Roy, Y. Sohn, D. Pradhan, *ACS Nano* **2013**, *7*, 2532.
[68] X. Zhao, W. Jin, J. Cai, J. Ye, Z. Li, Y. Ma, J. Xie, L. Qi, *Adv. Funct. Mater.* **2011**, *21*, 3554.
[69] C. Di Valentin, G. Pacchioni, A. Selloni, *J. Phys. Chem. C* **2009**, *113*, 20543.
[70] C. Di Valentin, E. Finazzi, G. Pacchioni, A. Selloni, S. Livraghi, M. C. Paganini, E. Giamello, *Chem. Phys.* **2007**, *339*, 44.
[71] C. Di Valentin, G. Pacchioni, A. Selloni, S. Livraghi, E. Giamello, *J. Phys. Chem. B* **2005**, *109*, 11414.
[72] K. Ellmer, *Nat. Photonics* **2012**, *6*, 809.
[73] R. J. Betsch, *J. Cryst. Growth* **1986**, *77*, 210.
[74] B. H. Toby, *J. Appl. Crystallogr.* **2001**, *34*, 210.
[75] Casa Software Ltd. http://www.casaxps.com/, accessed: October, 2013.
[76] D. Briggs, M. P. Seah, *Practical Surface Analysis by Auger and X-ray Photoelectron Spectroscopy*, 2nd Ed., John Wiley and Sons, Chichester **1992**.
[77] G. Kresse, J. Furthmüller, *Comput. Mater. Sci* **1996**, *6*, 15.
[78] P. E. Blöchl, *Phys. Rev. B* **1994**, *50*, 17953.

[79] A. V. Krukau, O. A. Vydrov, A. F. Izmaylov, G. E. Scuseria, *J. Chem. Phys.* **2006**, *125*, 224106.
[80] J. P. Perdew, K. Burke, M. Ernzerhof, *Phys. Rev. Lett.* **1996**, *77*, 3865.
[81] D. O. Scanlon, G. W. Watson, *J. Mater. Chem.* **2011**, *21*, 3655.
[82] D. O. Scanlon, G. W. Watson, *Phys. Chem. Chem. Phys.* **2011**, *13*, 9667.
[83] D. Scanlon, B. Morgan, G. Watson, A. Walsh, *Phys. Rev. Lett.* **2009**, *103*, 096405.
[84] D. O. Scanlon, A. B. Kehoe, G. W. Watson, M. O. Jones, W. I. F. David, D. J. Payne, R. G. Egdell, P. P. Edwards, A. Walsh, *Phys. Rev. Lett.* **2011**, *107*, 246402.
[85] D. O. Scanlon, P. D. C. King, R. P. Singh, A. de la Torre, S. M. Walker, G. Balakrishnan, F. Baumberger, C. R. A. Catlow, *Adv. Mater.* **2012**, *24*, 2154.
[86] D. O. Scanlon, G. W. Watson, *J. Phys. Chem. Lett.* **2010**, *1*, 3195.
[87] M. Burbano, D. O. Scanlon, G. W. Watson, *J. Am. Chem. Soc.* **2011**, *133*, 15065.
[88] C. Freysoldt, J. Neugebauer, C. Van de Walle, *Phys. Rev. Lett.* **2009**, *102*, 016402.
[89] C. Freysoldt, J. Neugebauer, C. G. Van de Walle, *Phys. Status Solidi B* **2011**, *248*, 1067.
[90] S. Lany, A. Zunger, *Phys. Rev. B* **2008**, *78*, 235104.
[91] J. K. Burdett, T. Hughbanks, G. J. Miller, J. W. Richardson, J. V. Smith, *J. Am. Chem. Soc.* **1987**, *109*, 3639.
[92] V. Çelik, E. Mete, *Phys. Rev. B* **2012**, *86*, 205112.
[93] P. Deák, B. Aradi, T. Frauenheim, *Phys. Rev. B* **2011**, *83*, 155207.
[94] H. A. Huy, B. Aradi, T. Frauenheim, P. Deák, *Phys. Rev. B* **2011**, *83*, 155201.
[95] B. J. Morgan, D. O. Scanlon, G. W. Watson, *J. Mater. Chem.* **2009**, *19*, 5175.
[96] P. Deák, B. Aradi, T. Frauenheim, E. Janzén, A. Gali, *Phys. Rev. B* **2010**, *81*, 153203.